

Room-temperature high spin-orbit torque due to quantum confinement in sputtered $\text{Bi}_x\text{Se}_{(1-x)}$ films

Mahendra DC¹, Roberto Grassi², Jun-Yang Chen², Mahdi Jamali², Danielle Reifsnnyder Hickey³, Delin Zhang², Zhengyang Zhao², Hongshi Li³, P. Quarterman², Yang Lv², Mo Li², Aurelien Manchon^{4,5}, K. Andre Mkhoyan³, Tony Low² and Jian-Ping Wang^{1,2,3*}

The spin-orbit torque (SOT) that arises from materials with large spin-orbit coupling promises a path for ultralow power and fast magnetic-based storage and computational devices. We investigated the SOT from magnetron-sputtered $\text{Bi}_x\text{Se}_{(1-x)}$ thin films in $\text{Bi}_x\text{Se}_{(1-x)}/\text{Co}_{20}\text{Fe}_{60}\text{B}_{20}$ heterostructures by using d.c. planar Hall and spin-torque ferromagnetic resonance (ST-FMR) methods. Remarkably, the spin torque efficiency (θ_s) was determined to be as large as 18.62 ± 0.13 and 8.67 ± 1.08 using the d.c. planar Hall and ST-FMR methods, respectively. Moreover, switching of the perpendicular CoFeB multilayers using the SOT from the $\text{Bi}_x\text{Se}_{(1-x)}$ was observed at room temperature with a low critical magnetization switching current density of $4.3 \times 10^5 \text{ A cm}^{-2}$. Quantum transport simulations using a realistic sp^3 tight-binding model suggests that the high SOT in sputtered $\text{Bi}_x\text{Se}_{(1-x)}$ is due to the quantum confinement effect with a charge-to-spin conversion efficiency that enhances with reduced size and dimensionality. The demonstrated θ_s , ease of growth of the films on a silicon substrate and successful growth and switching of perpendicular CoFeB multilayers on $\text{Bi}_x\text{Se}_{(1-x)}$ films provide an avenue for the use of $\text{Bi}_x\text{Se}_{(1-x)}$ as a spin density generator in SOT-based memory and logic devices.

A new class of quantum materials known as topological insulators (TIs) is of great interest due to their ability to convert charge into non-equilibrium spin density efficiently^{1–6}. Efficient charge-to-spin density conversion has been predicted theoretically^{1,2} and realized experimentally in TIs^{7,8}. The surface spin polarization in TIs is observed directly using angle-resolved photoemission spectroscopy^{9,10} and an electrical method^{7,8}, and also indirectly by depositing a ferromagnet (FM) layer on top of TIs via a spin-orbit torque (SOT)^{3–6,11}. Additionally, the conversion of spin-to-charge current is also observed by pumping spin from a FM layer to a TI layer^{12–15}. The figure-of-merit of charge-to-spin density conversion known as spin torque efficiency (θ_s), which is defined as the ratio of the spin conductivity (σ_s , which measures the spin torque strength) to the charge conductivity (σ), can be larger than 100% even in imperfect TIs^{3–5,12}. This efficient spin density generation in TIs is due to the perpendicular locking of an electron's spin with its momentum^{1,3,7,8,12}. In addition to the spin-momentum locking, a bulk effect known as the spin Hall effect^{16,17} and the interfacial Rashba effect^{18–20} can also generate spin density in TIs, as well as in heavy metals (HMs). Conventionally, the spin density is due to the absorption of spin current generated by using a FM polarizer that transfers its spin angular momentum to another FM layer, which is the mechanism for spin-transfer torque (STT)^{21,22}. SOT-based memory and logic devices are superior to STT-based devices because they do not require a separate polarizer for the generation of spin density and can generate spin density much more efficiently^{16,23–25}. The use of TIs as spin density generators in SOT-based spintronic devices could potentially lead to a lower writing current density, and thus a significantly improved energy efficiency and much better device reliability.

The most commonly studied spin density generators in non-magnetic (NM) and FM material heterostructures are HMs, such as Ta^{16,26,27}, W^{24,28}, Pt^{19,29}, and TIs, such as Bi_2Se_3 (refs 3,6,12), $(\text{Bi}_{(1-x)}\text{Sb}_x)_2\text{Te}_3$ (refs 4,5), Bi_2Te_3 (ref. 5) and so on. The key practical application of these spin density generators is to switch the magnetization via the SOT, which has been achieved in HM/FM heterostructures with a switching current density (J_{sw}) on the order of 10^6 – 10^8 A cm^{-2} at room temperature (RT)^{16,19,29}. In addition to HMs, the switching of a magnetically doped TI ($\text{Cr}_{0.08}\text{Bi}_{0.54}\text{Sb}_{0.38}$)₂Te₃ layer at 1.9 K has also been observed via SOT from TI, but with a much lower J_{sw} ($8.9 \times 10^4 \text{ A cm}^{-2}$) (ref. 4). RT switching of perpendicular CoTb (ref. 30) and in-plane NiFe (ref. 31) layers has been reported via SOT from Bi_2Se_3 with a J_{sw} of 3.0×10^6 and $5 \times 10^5 \text{ A cm}^{-2}$, respectively. However, all these crystalline TI samples are grown on a single-crystal substrate using molecular beam epitaxy.

In this paper, we report $\text{Bi}_x\text{Se}_{(1-x)}$ films with high SOTs at RT grown onto thermally oxidized silicon substrates by magnetron sputtering, which is a compatible process in the semiconductor industry. The d.c. planar Hall³² and spin-torque ferromagnetic resonance (ST-FMR) methods were used for the characterization of the SOT in $\text{Bi}_x\text{Se}_{(1-x)}/\text{CoFeB}$ heterostructures with in-plane CoFeB. At RT, the θ_s of the sputtered $\text{Bi}_x\text{Se}_{(1-x)}$ film is up to two orders of magnitude larger than that of HMs. Notably, we developed perpendicular CoFeB multilayers on $\text{Bi}_x\text{Se}_{(1-x)}$ films, and we demonstrated the switching of the magnetization using the SOT that arises from the $\text{Bi}_x\text{Se}_{(1-x)}$ with a very low J_{sw} in bilayers at RT. Moreover, σ_s , which is the product of the θ_s and σ of the NM, is determined to be comparable to or larger than previously reported values of other spin density generators^{3,6,16,33}. The sputter-deposited $\text{Bi}_x\text{Se}_{(1-x)}$ has a

¹School of Physics and Astronomy, University of Minnesota, Minneapolis, MN, USA. ²Department of Electrical and Computer Engineering, University of Minnesota, Minneapolis, MN, USA. ³Department of Chemical Engineering and Materials Science, University of Minnesota, Minneapolis, MN, USA.

⁴King Abdullah University of Science and Technology (KAUST), Physical Science and Engineering Division (PSE), Thuwal, Saudi Arabia. ⁵King Abdullah University of Science and Technology (KAUST), Computer, Electrical and Mathematical Sciences and Engineering Division (CEMSE), Thuwal, Saudi Arabia.

*e-mail: jpwang@umn.edu

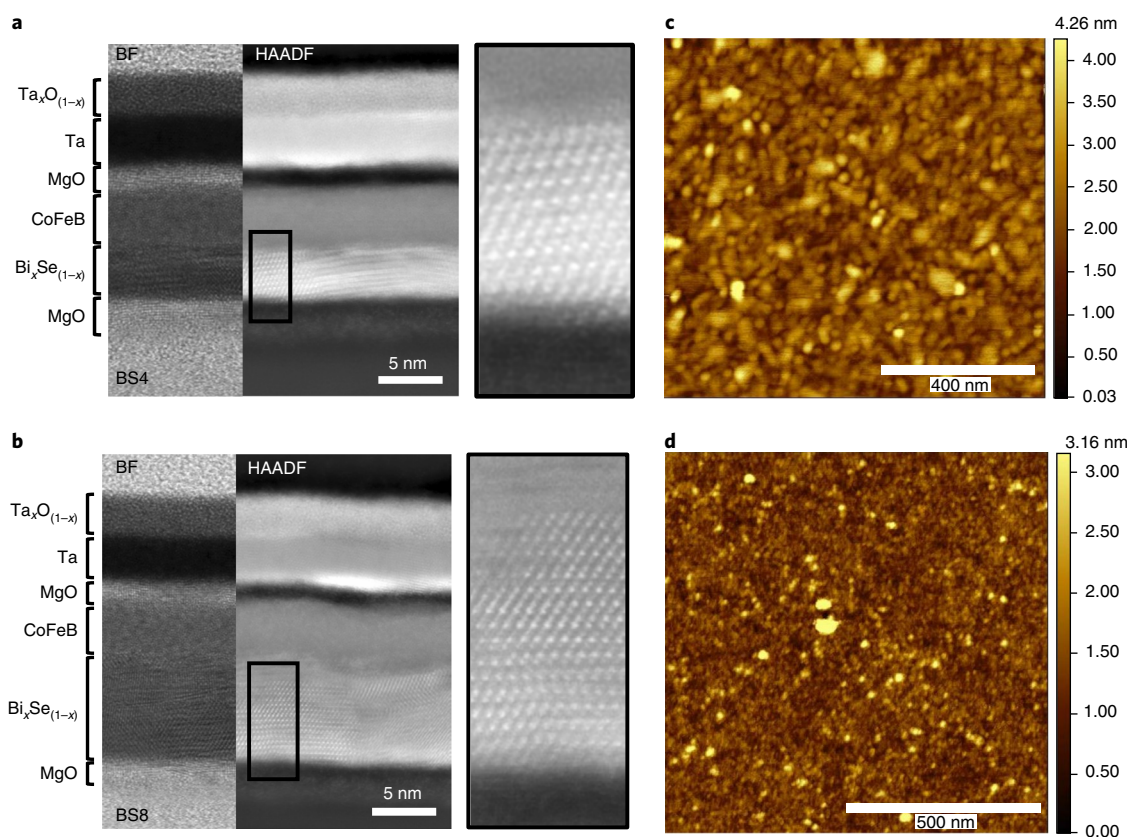


Fig. 1 | STEM and surface morphology characterization. **a,b**, Composites of simultaneously acquired bright-field STEM and HAADF-STEM images of samples BS4 (**a**) and BS8 (**b**). The selected regions of the HAADF-STEM images indicated by black rectangles are magnified on the right to show the $\text{Bi}_x\text{Se}_{(1-x)}$ atomic detail. **c,d**, The AFM images are of the 4 nm $\text{Bi}_x\text{Se}_{(1-x)}$ (**c**) and sample BS4 (**d**).

granular structure with a grain size as small as approximately 6 nm. Analysis of the electronic band structure indicates that the reduced dimensionality and quantum confinement strongly influences the spintronic properties of the TI. Our theory identifies the presence of lowly dispersive surface bands with a large charge-to-spin conversion efficiency in nanoscale grains, which might explain the experimentally observed enhancement in the figure of merit θ_s .

Structural characterization

To characterize the SOT that arises from the $\text{Bi}_x\text{Se}_{(1-x)}$ films, thin films with the multilayer structure $\text{Si}/\text{SiO}_2/\text{MgO}(2\text{ nm})/\text{Bi}_x\text{Se}_{(1-x)}(t_{\text{BS}}\text{ nm})/\text{CoFeB}(5\text{ nm})/\text{MgO}(2\text{ nm})/\text{Ta}(5\text{ nm})$ were prepared, with $t_{\text{BS}} = 4, 6, 8, 16$ and 40 nm . Unless otherwise stated, we use the labels BS4, BS6, BS8, BS16 and BS40 for the samples with $t_{\text{BS}} = 4, 6, 8, 16$ and 40 nm , respectively. The high-angle annular dark-field scanning transmission electron microscopy (HAADF-STEM) images of samples BS4 and BS8 (Fig. 1a,b, respectively) show that $\text{Bi}_x\text{Se}_{(1-x)}$ has a polycrystalline structure and that the atomic layers of Bi and Se are continuous in both samples. Additionally, the average grain orientation in sample BS4 is 2° with a standard deviation of 9° (from the vertical c orientation), which is almost identical to the average grain orientation in sample BS8 (2° with a standard deviation of 8°). The average size of the grains in sample BS4 is approximately 6 nm wide and 4 nm high, whereas that of the grains in sample BS8 is approximately 18 nm wide and 8 nm high. Figure 1c shows the atomic force microscopy (AFM) images of a $\text{Si}/\text{SiO}_2/\text{MgO}(2\text{ nm})/\text{Bi}_x\text{Se}_{(1-x)}(4\text{ nm})$ film. The root mean square (r.m.s.) value of the surface roughness of the 4 nm $\text{Bi}_x\text{Se}_{(1-x)}$ film is 0.5 nm. Furthermore, we probed the surface roughness propagation in the full stack, as shown in Fig. 1d. The r.m.s. value of 0.38 nm for the surface roughness in sample BS4 confirms the smoothness of the

full stack, which is necessary for future device fabrication on a wafer level (Supplementary Fig. 8).

SOT characterization

The multilayer thin films with in-plane magnetization (M) were patterned into Hall-cross bars with dimensions $5\text{--}30\text{ }\mu\text{m}$ wide and $70\text{ }\mu\text{m}$ long, and a d.c. planar Hall measurement was performed on the Hall-cross bar with dimensions $10\text{ }\mu\text{m} \times 70\text{ }\mu\text{m}$, as shown in Fig. 2b. The bipolar input current of magnitude up to 8.5 mA was injected along the x direction, and the angle-dependent Hall resistance ($R_{\text{H}}(I, \alpha)$, where I is input current and α is the angle between the current flow direction and external field) was measured under the application of a constant 5,000 Oe in-plane magnetic field while rotating the sample in the xy plane from -7 to 365° . The in-plane SOT exerted by the accumulated spin density on the interface of the $\text{Bi}_x\text{Se}_{(1-x)}/\text{CoFeB}$ (Fig. 2a) is obtained by using the Slonczewski's equation²¹, $\tau_{\parallel} = \frac{\hbar J_s}{2eM_s t_{\text{FM}}} [\hat{\mathbf{m}} \times (\hat{\sigma} \times \hat{\mathbf{m}})]$, where \hbar is the reduced Planck's constant, J_s is the effective spin-polarized current density, e is an electronic charge, M_s is the saturation magnetization, t_{FM} is the thickness of the FM layer, $\hat{\mathbf{m}}$ is the magnetization unit vector and $\hat{\sigma}$ is the unit vector of the current-induced spin polarization on the interface. The effective out-of-plane magnetic field associated with the in-plane torque (τ_{\parallel}) is given by¹⁶ $H_{\text{OOP}} = \frac{\hbar J_s}{2eM_s t_{\text{FM}}} (\hat{\sigma} \times \hat{\mathbf{m}})$. In addition to the τ_{\parallel} , there is also an out-of-plane component of SOT due to the spin density at the interface, which is given by $\tau_{\perp} \propto (\hat{\sigma} \times \hat{\mathbf{m}})$. The in-plane magnetic field associated with the out-of-plane torque (τ_{\perp}) is given by $H_{\text{T}} \propto \hat{\sigma}$. Furthermore, there is also τ_{\perp} due to the Oersted field (H_{Oe}) generated by charge current flow in the NM layer. Figure 2c shows $R_{\text{H}}(I, \alpha)$ for the sample BS4 at $\pm 8.5\text{ mA}$. In principle, $R_{\text{H}}(I, \alpha)$ consists of the planar Hall resistance (R_{PHE}) and

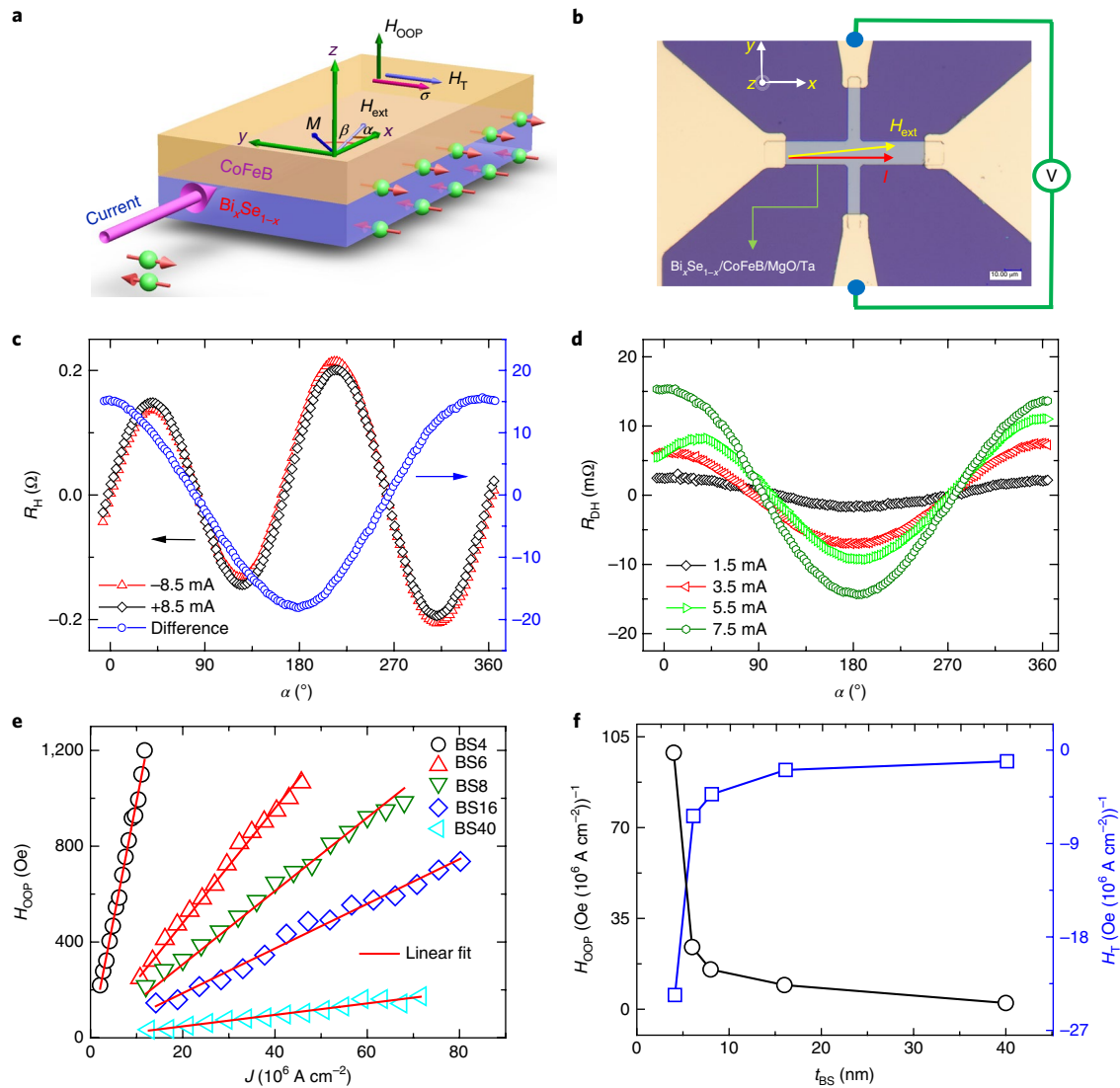


Fig. 2 | Schematic diagram, experimental set-up, angle-dependent Hall resistance measurements and characterization of SOT. a, A 3D schematic diagram demonstrating the SOT in a $\text{Bi}_x\text{Se}_{1-x}/\text{CoFeB}$ heterostructure. H_{ext} is the in-plane externally applied magnetic field. The red arrows represent the direction of spin-magnetic moment. **b**, An optical micrograph of the fabricated Hall-cross bar with schematic drawings of the Hall measurement set-up. **c**, The $R_{\text{H}}(I, \alpha)$ of sample BS4 at ± 8.5 mA input current on the left axis and $R_{\text{DH}}(I, \alpha)$ on the right axis at RT under a constant 5,000 Oe in-plane magnetic field. **d**, The $R_{\text{DH}}(I, \alpha)$ at different input currents for the BS4 sample. **e**, The variation of H_{OOP} with the current density. **f**, The variation of H_{OOP} (left axis) and H_{T} (right axis) as a function of $\text{Bi}_x\text{Se}_{1-x}$ thickness.

the anomalous Hall resistance (R_{AHE}) due to the planar and anomalous Hall effects, respectively. The R_{PHE} is due to the combined effects of the external field, current-induced effective fields and the anisotropy field that acts on the magnetization ($R_{\text{PHE}} \propto \sin(2\beta)$, where β is the angle between the magnetization and current flow direction). R_{AHE} is due to the pulling of the magnetization in the out-of-plane direction by a current-induced effective field ($R_{\text{AHE}} \propto M_z$, where M_z is the z component of the magnetization).

The effective current-induced transverse and out-of-plane magnetic fields H_{T} and H_{OOP} , respectively, can be extracted by characterizing $R_{\text{H}}(I, \alpha)$ for the positive and negative input currents. The difference of the Hall resistances is given by³²:

$$R_{\text{DH}}(I, \alpha) = 2R_{\text{PHE}} \frac{(H_{\text{T}} + H_{\text{Oe}})}{H_{\text{ext}}} (\cos \alpha + \cos 3\alpha) + 2 \frac{dR_{\text{AHE}}}{dH} H_{\text{OOP}} \cos \alpha + C \quad (1)$$

where C is the resistance offset that accounts for the Hall bar imbalance, $\frac{dR_{\text{AHE}}}{dH}$ is the gradient of the change in the anomalous Hall signal versus the externally applied out-of-plane magnetic field. Figure 2d shows $R_{\text{DH}}(I, \alpha)$ versus an externally applied field angle for the sample BS4 at different input currents. The $R_{\text{DH}}(I, \alpha)$ increases with an increase in the input current and has a maximum located at approximately 180° . $\frac{dR_{\text{AHE}}}{dH}$ is obtained by sweeping the out-of-plane field at a small 1 mA input current. After considering current-shunting and short-circuit effects³⁴, $\frac{dR_{\text{AHE}}}{dH}$ is determined to be $6.75, 7.33, 7.37, 7.55$ and $6.51 \times 10^{-4} \Omega \text{Oe}^{-1}$ for samples BS4–BS40, respectively. The H_{Oe} is estimated by using Ampere's law after knowing the charge current in the NM layer using a one-dimensional (1D) current-shunting equation (details in Supplementary Section 2). The R_{PHE} is obtained by fitting $R_{\text{DH}}(I, \alpha)$ data to the equation $R_0 + R_{\text{AHE}} \cos(\alpha) + R_{\text{PHE}} \sin(2\alpha)$, where R_0 is resistance offset. After determining R_{PHE} , $\frac{dR_{\text{AHE}}}{dH}$, and H_{Oe} values, H_{OOP}

Table 1 | A summary of the θ_s , σ_s , J_{sw} , σ and switching power dissipation of the TIs and HMs in this work and the best previous reports at RT

| Parameters | $\text{Bi}_x\text{Se}_{(1-x)}$ (this work) | Bi_2Se_3 (ref. ³⁰) | Bi_2Se_3 (ref. ³¹) | $\beta\text{-Ta}$ (ref. ¹⁶) | Pt (refs ^{19,29}) |
|---|--|--|--|---|---------------------------------|
| σ ($\Omega^{-1}\text{m}^{-1}$) | 0.78×10^4 | 9.43×10^4 | 2.43×10^4 | 5.3×10^5 | 4.2×10^6 |
| σ_s ($10^5 \frac{\hbar}{2e} \Omega^{-1}\text{m}^{-1}$) | 1.5 | 0.15 | 0.43 | -0.8 | 3.4 |
| θ_s | 18.62 | 0.16 | 1.75 | -0.15 | 0.08 |
| J_{sw} (A cm^{-2}) | 4.3×10^{5a} | 3×10^6 | 6×10^5 | 5.5×10^6 | $2.85 \times 10^7\text{--}10^8$ |
| Switching power dissipation ($\frac{J_{sw}^2}{\sigma}$ W m^{-3}) | 1.29×10^{15a} | 9.54×10^{15} | 1.48×10^{15} | 5.7×10^{15} | 1.93×10^{16} |
| Symmetry breaking external in-plane magnetic field (Oe) | 80^a | 1,000 | 0 | 100 | 100 |
| Switched magnetic system | CoFeB/Gd/CoFeB Out-of-plane | CoTb Out-of-plane | NiFe In-plane | CoFeB Out-of-plane | Co Out-of-plane |

^aThese results are of switching the $\text{Bi}_x\text{Se}_{(1-x)}$ sample. Note that J_{sw} is the current density only through the NM layer.

and H_T can be determined by curve fitting of the $R_{\text{DH}}(I, \alpha)$ experimental data to equation (1). The H_{OOP} versus the current density is presented in Fig. 2e. The $\frac{H_{\text{OOP}}}{J_{\text{BS}}}$ determined by the linear fit is as large as 98.83 ± 0.7 Oe per 10^6 A cm^{-2} for sample BS4, where J_{BS} is the current density in the $\text{Bi}_x\text{Se}_{(1-x)}$ layer (the uncertainty is the standard error from the linear fit). The spin torque efficiency $\theta_s = \frac{2eM_s J_{\text{FM}} H_{\text{OOP}}}{\hbar J_{\text{BS}}}$ of sample BS4 is determined to be 18.62 ± 0.13 . Sample BS4 has the largest θ_s value at RT reported to date, which means that it is the most efficient spin-torque generator at RT. The $\frac{H_{\text{OOP}}}{J_{\text{BS}}}$ values for samples BS6–BS40 are 23.96 ± 0.19 , 15.32 ± 0.16 , 9.32 ± 0.11 and 2.39 ± 0.05 Oe per 10^6 A cm^{-2} , respectively. The θ_s for samples BS6–BS40 are determined to be 4.50 ± 0.03 , 2.88 ± 0.03 , 1.75 ± 0.02 and 0.45 ± 0.01 , respectively. The σ_s is determined to be as large as $1.45 \pm 0.01 \times 10^5 \frac{\hbar}{2e} \Omega^{-1}\text{m}^{-1}$ for sample BS4. The $\text{Bi}_x\text{Se}_{(1-x)}$ films have both σ and σ_s values comparable to those from previous reports on TIs^{3,4,12,35}. A summary of σ , θ_s and σ_s for our samples and the best previously reported TIs and HMs are presented in Table 1.

At a smaller in-plane field of approximately 200 Oe, which is sufficient to saturate the magnetization along the in-plane direction, H_T is estimated to be 23.60 ± 0.04 Oe per 10^6 A cm^{-2} in sample BS4 (Supplementary Fig. 3b) after considering the contribution from H_{Oe} . The H_T results for samples BS4–BS40 are presented in Fig. 2f. The positive τ_{\perp} in sputtered $\text{Bi}_x\text{Se}_{(1-x)}$ indicates that the Rashba–Edelstein-induced τ_{\perp} is absent, which is consistent with the previous reports on crystalline Bi_2Se_3 (refs ^{3,6}). Experimentally, we observed that, as the thickness of the $\text{Bi}_x\text{Se}_{(1-x)}$ film increases, the grain size also increases and the magnitudes of the τ_{\parallel} and τ_{\perp} decrease (Fig. 2f). This gives a clear indication of the influence of grain size on the SOT in sputtered $\text{Bi}_x\text{Se}_{(1-x)}$ films.

In addition to the d.c. planar Hall measurement, we also performed ST-FMR measurements on samples $\text{Si/SiO}_2/\text{MgO}(2\text{ nm})/\text{Bi}_x\text{Se}_{(1-x)}(4\text{ and }16\text{ nm})/\text{CoFeB}(5\text{ nm})/\text{MgO}(2\text{ nm})/\text{Ta}(1\text{ nm})$ to validate the high charge-to-spin conversion from the sputtered $\text{Bi}_x\text{Se}_{(1-x)}$ films^{3,5,36} (details in Supplementary Section 4). The θ_s values obtained by performing the ST-FMR measurement for the $\text{Bi}_x\text{Se}_{(1-x)}$ 4 and 16 nm samples are 8.67 ± 1.08 and 1.56 ± 0.01 , respectively. The sign of the θ_s is in agreement with the previous reports on crystalline Bi_2Se_3 (refs. ^{3,6,12}) and opposite to that of the Ta. The θ_s values obtained from the ST-FMR measurement are similar to those determined by using the d.c. planar Hall measurement. Given that previous reports of the θ_s values of TIs show a large variability^{3,6,12,14}, we emphasize that our θ_s values determined by the d.c. planar Hall and ST-FMR methods are in good agreement.

Spin-accumulation enhanced by quantum confinement

A defining feature of our sputtered $\text{Bi}_x\text{Se}_{(1-x)}$ film is its granular nature with a grain size down to the order of nanometres, and the reduced dimensionality can have a strong influence on the electronic properties³⁷. In Fig. 3a, we show the evolution of the band structure as dimensionality is reduced from that of a four quintuple layer (4QL) slab to its nanowire counterpart with the cross-section illustrated in the inset of Fig. 3b. The electronic structure was modelled using an atomistic sp^3 tight-binding Hamiltonian, which reproduces accurately the bulk band structure of Bi_2Se_3 obtained from ab initio calculations³⁸. Electronic bands of the wire revealed additional states that are not within the energy spectrum of the slab (grey shaded region in Fig. 3a). Analysis of the wavefunctions (Fig. 3e) affirmed that the additional bands have a surface character and are localized mainly on the wire sidewalls and corners. The surface states exhibit robust spin-momentum locking, as shown by the colour plot in Fig. 3a, in which the colour denotes the projected in-plane spin density (S_y) on the top (111) surface of the nanowire. More precisely, using matrix notation:

$$S_{y,v} = \psi_v^\dagger P \otimes \sigma_y \psi_v$$

with P is the projector matrix to the atomic orbitals belonging on the top surface, σ_y is one of the three Pauli matrices and ψ_v is the normalized wavevector that corresponds to the quantum number v (we use normalized units with respect to $\hbar/2$). Here, only S_y values for the forward propagating states (positive group velocity v_x) are shown, with the dominant contribution coming from the lowly dispersive surface bands.

In the case of a nanodot, the electronic band structure consists of discrete energy states that are best visualized through its density of states as shown in Fig. 3b (Methods). We found a close similarity between the wire and dot spectra. In both cases, the density-of-states spectrum is enhanced in the energy window 0.3–0.9 eV compared to the slab case. In addition, some of the quasi-singularities in the spectrum of the wire persist in the nanodot spectrum at similar energies. This clearly indicates that the additional lowly dispersive states of the wire survive in the dot geometry. These states also produce an enhanced surface S_y spectrum, as shown in Fig. 3c. Here, the total contribution (per unit area) of states at energy E is considered, for example, in the dot case:

$$S_y^+(E) = \frac{1}{L_x L_y} \sum_{v, v_x > 0} \delta(E - \epsilon_v) S_{y,v}$$

where $L_{x,y}$ are the dot dimensions in the x and y directions, δ is Dirac's delta function, ϵ_v is the energy eigenvalue that corresponds to ψ_v .

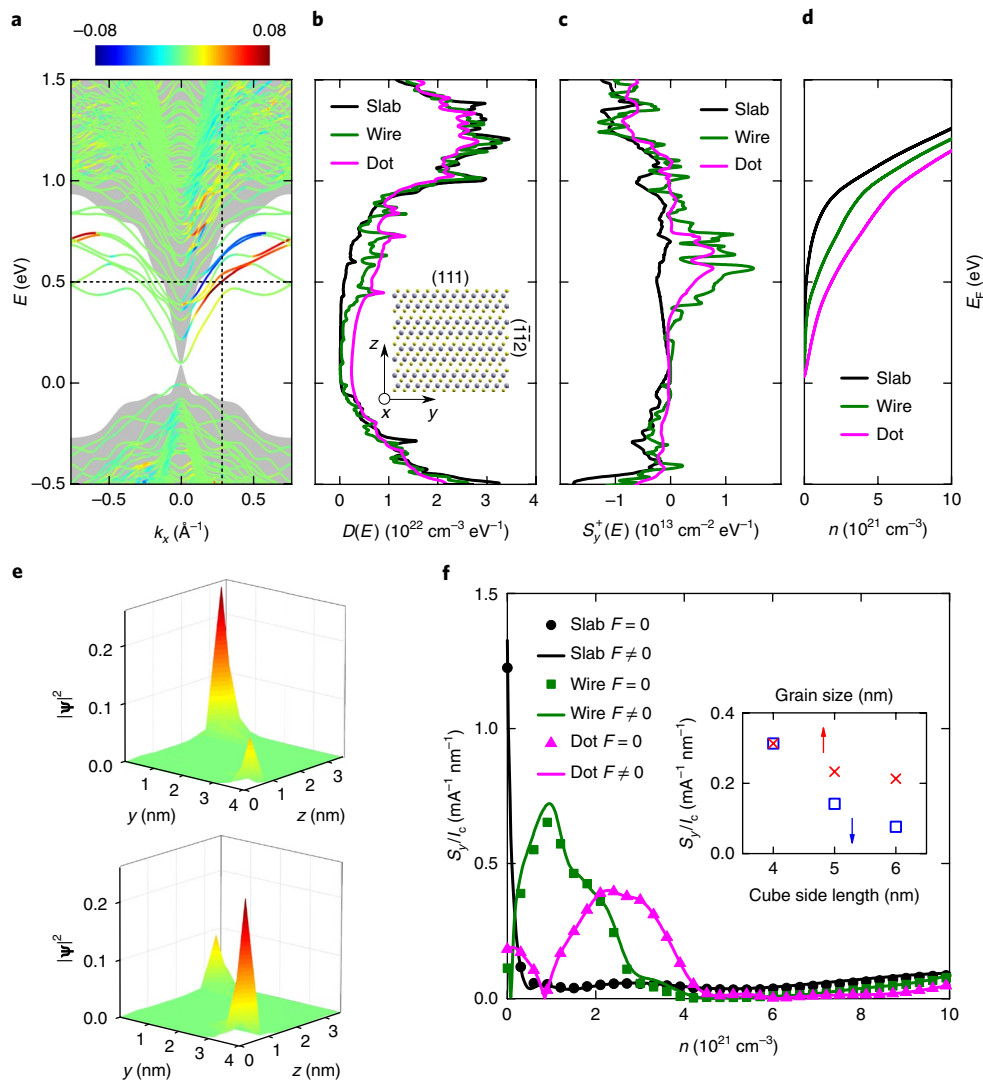


Fig. 3 | Effect of quantum confinement on spin accumulation. **a**, Band structure of a slab (grey shaded region) and a square wire (lines) with a thickness of 4 QLs. The colours represent the projected spin density (y component) on the top surface of forward propagating states. **b**, Density of states versus (vs) energy for the slab, wire and a cubic dot with the same thickness of 4 QLs. Inset: cross-section view of the wire atomic structure. **c**, Total projected spin density on the top surface of forward propagating states vs energy. **d**, Carrier density vs Fermi energy at 300 K. **e**, Two degenerate and orthogonal wavefunctions of the wire that correspond to the energy and \mathbf{k} vector indicated by the dashed lines in **a**. **f**, Charge-to-spin conversion efficiency, that is, the ratio between spin accumulation at the top surface and charge current as a function of carrier concentration calculated in the linear response with or without an applied electric field F . Inset: conversion efficiency of the dot geometry, averaged over the range of carrier densities (n) 1×10^{21} to $3 \times 10^{21} \text{ cm}^{-3}$ and plotted as a function of confinement size, for dots with cubic shape (blue symbols) and for dots with the same thickness as 4QLs in the z direction and different size in the xy plane (red symbols).

and the sum is restricted to forward propagating states. We verified that the x and z components of the spin polarization of the top surface are typically smaller in all three geometries. The non-equilibrium spin polarization due to an applied current in an electron gas is also known as the Edelstein effect³⁹. As we elaborate below, we suggest that the additional lowly dispersive surface states due to the quantum confinement effect is the reason for the high charge-to-spin conversion in our nanoscale granular sputtered $\text{Bi}_2\text{Se}_{(1-x)}$ (refs 40–43). In this context, the intraband transitions at the Fermi level produce the τ_{\perp} , whereas interband transitions in the Fermi sea, associated with the Berry curvature of the surface states⁴⁴, produces the τ_{\parallel} (refs 40,41). In the present model, we focus on the intraband-driven Edelstein effect. Experimentally, it is also likely that defects or surface reconstruction might lead to a built-in electric field, which can produce Rashba split bands⁴⁵ and lead to additional

contributions due to the Rashba–Edelstein effect. However, due to the sub-10 nm nanoscale grain sizes in our experiments, the size confinement has a stronger influence on the energy spectrum.

To investigate this idea, we evaluated the quantum spin transport properties of a 2D array of Bi_2Se_3 grains of varying sizes that ranged from 4 to 6 nm, as shown in Fig. 3f. The crystal orientation of these nanograins along the x , y and z directions are $[\bar{1}10]$, $[\bar{1}12]$ and $[111]$, respectively. We considered electrical current that flowed in the x direction using the standard non-equilibrium Green function approach (details of the simulations in Methods). For comparison, we also considered the slab and wire counterparts of a dot with a thickness of 4 nm.

In Fig. 3f, we plot as a function of carrier density the ratio between S_y and charge current I_c (Methods), which can be interpreted as a measure of the charge-to-spin conversion. The conversion

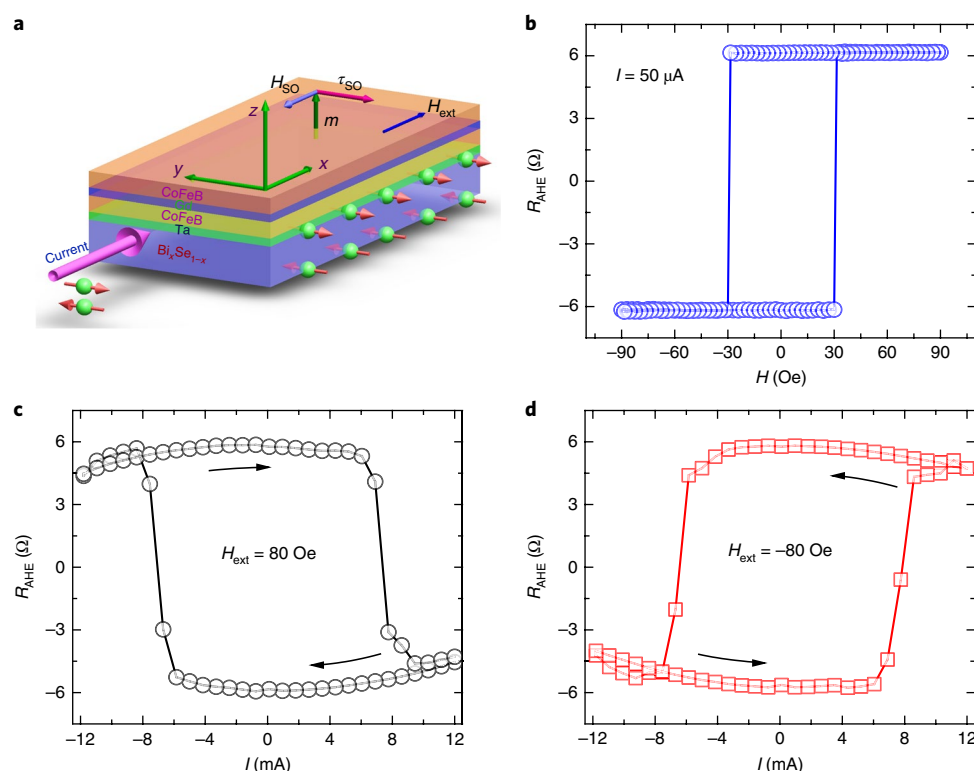


Fig. 4 | Current-induced magnetization switching in the $\text{Bi}_x\text{Se}_{1-x}$ (4 nm)/Ta (0.5 nm)/CoFeB (0.6 nm)/Gd (1.2 nm)/CoFeB (1.1 nm) heterostructure. **a, Schematic of the switching sample stack structure, where H_{SO} and τ_{SO} are current-induced spin-orbit field and spin-orbit torque, respectively. **b**, R_{AHE} measured in the $\text{Bi}_x\text{Se}_{1-x}$ switching sample using a current of 50 μA . **c,d**, Current-induced switching of the magnetization due to the SOT that arises from the $\text{Bi}_x\text{Se}_{1-x}$ underlayer in the presence of constant 80 Oe (**c**) and -80 Oe (**d**) in-plane bias fields. The Hall-cross bar with dimensions $15 \times 70 \mu\text{m}$ was used for the switching experiment.**

between carrier density and the Fermi level position in energy is provided in Fig. 3d. Compared to the slab, the wire and dot geometries provide better performances in the range of carrier densities between 3×10^{20} and $3 \times 10^{21} \text{ cm}^{-3}$, which also coincides with the experimental observation (Supplementary Section 1). The enhancement can be traced back to the peaks in spin density spectrum that occur at about 0.55 eV (Fig. 3c). When the size of the dot is increased from 4 to 6 nm, the average conversion ratio is decreased (Fig. 3f inset), in agreement with the trend observed for $\frac{H_{\text{T}}}{J_{\text{BS}}}$ in the experiment (Fig. 2f). A similar trend was observed when the thickness was kept fixed at 4 nm and only the in-plane size (grain size) was increased, which can be explained by the fact that the surface states localized at the edges with the (112) surfaces (Fig. 3e) become less densely packed. These results suggest that SOT efficiencies can be enhanced by reducing size and dimensionality of the TI. Although our calculations considered only the intraband current-driven spin density responsible for τ_{\perp} , it is reasonable to speculate that the interband spindensity—not calculated in this model—should also be enhanced. As a matter of fact, the interband contribution is a correction to the intraband Edelstein effect that arises from the precession of the non-equilibrium spin accumulation about the magnetization⁴³. Therefore, the enhancement of the intraband Edelstein effect by quantum confinement is expected to be accompanied by a corresponding enhancement of the interband contribution. Our modelling is limited to ideal structures with a Bi_2Se_3 composition and a regular rectangular shape. The disordered nature of the experimental sputtered $\text{Bi}_x\text{Se}_{1-x}$ (in which the stoichiometric ratio deviates from that of Bi_2Se_3 and the granular shape is irregular) might also influence the charge-to-spin conversion mechanism. For example, in Supplementary Fig. 10, we show

that the influence on charge-to-spin conversion due to different crystal orientations.

Current-induced perpendicular CoFeB multilayer switching

The SOT that arises from $\text{Bi}_x\text{Se}_{1-x}$ can be directly observed by switching a FM with perpendicular magnetic anisotropy (PMA) in close proximity to the spin channel^{16,19,27,29}. We prepared a $\text{Si}/\text{SiO}_2/\text{MgO}$ (2 nm)/ $\text{Bi}_x\text{Se}_{1-x}$ (4 nm)/Ta (0.5 nm)/CoFeB (0.6 nm)/Gd (1.2 nm)/CoFeB (1.1 nm)/MgO (2 nm)/Ta (2 nm) switching sample (labelled as $\text{Bi}_x\text{Se}_{1-x}$ switching sample), as shown schematically in Fig. 4a, and a control switching sample with $\text{Bi}_x\text{Se}_{1-x}$ (4 nm) replaced by Ta (4.5 nm) for the switching experiment, labelled as the Ta switching sample. Figure 4b shows the R_{AHE} loop of the $\text{Bi}_x\text{Se}_{1-x}$ switching sample obtained by sweeping the out-of-plane field at a constant input current of 50 μA . The non-zero R_{AHE} at zero magnetic field confirms the easy axis of the magnetization along the out-of-plane direction. Additionally, PMA in the switching $\text{Bi}_x\text{Se}_{1-x}$ sample was confirmed by performing a vibrating sample magnetometry (VSM) measurement (Supplementary Fig. 1d). The R_{AHE} loops of the $\text{Bi}_x\text{Se}_{1-x}$ switching sample that resulted from a current sweep under the application of a constant +80 Oe and -80 Oe field along the current channel are displayed in Fig. 4c,d, respectively. The magnetization switching occurs at approximately $\pm 7.2 \text{ mA}$ ($\sim 4.3 \times 10^5 \text{ A cm}^{-2}$), as shown in Fig. 4c,d. Upon changing the polarity of the external field, the chirality of the R_{AHE} loop changes, which is consistent with the results of previous reports^{16,27,29}. The magnetization switching of the Ta switching sample (details in Supplementary Section 8) occurs at approximately $\pm 24.6 \text{ mA}$ ($\sim 2.0 \times 10^7 \text{ A cm}^{-2}$). A comparison between the SOT switching power dissipation ($\frac{I_{\text{sw}}^2}{\sigma}$) in our switching $\text{Bi}_x\text{Se}_{1-x}$ sample, recent reports on Bi_2Se_3 and the best previously

reported results on HMs are presented in Table 1. The switching power dissipation in our $\text{Bi}_x\text{Se}_{(1-x)}$ switching sample is approximately one order of magnitude smaller than those in $\text{Bi}_2\text{Se}_3/\text{CoTb}$ (ref. ³⁰) and Pt/Co (refs ^{19,29}), whereas it is comparable with that of the in-plane $\text{Bi}_2\text{Se}_3/\text{NiFe}$ (ref. ³¹). To study the effect of thin Ta insertion layer in the $\text{Bi}_x\text{Se}_{(1-x)}$ switching sample, θ_s of $\text{Bi}_x\text{Se}_{(1-x)}$ (4 nm)/Ta (0.5 nm) stack was measured. In the PMA sample, the same device that is used for switching can be used for θ_s measurements by utilizing the second harmonic Hall⁴⁶ current-induced hysteresis loop shift^{30,47,48} along with anomalous Hall resistance^{16,27,28} measurement techniques. These techniques yielded comparable values of θ_s (refs ^{16,26–28,46–48}). In our case, θ_s of the switching $\text{Bi}_x\text{Se}_{(1-x)}$ sample was determined to be 6.0 ± 0.1 using the second harmonic Hall method (details in Supplementary Section 6). Furthermore, we also performed ST-FMR measurements by replacing the perpendicular CoFeB/Gd/CoFeB by a single in-plane CoFeB (5 nm) layer to study the effect of the Ta(0.5 nm) insertion layer, as well as if there was any contribution of the Gd layer to the SOT. The θ_s obtained by ST-FMR was 1.35 ± 0.06 . The θ_s decreased significantly due to the insertion of the Ta(0.5 nm) layer to get PMA in the $\text{Bi}_x\text{Se}_{(1-x)}$ switching sample as compared to the in-plane sample BS4. The additional $\text{Bi}_x\text{Se}_{(1-x)}$ /Ta interface dissipates spin density due to the spin-flip scattering⁴⁹. Ta has a spin-diffusion length larger than 0.5 nm, but there is still a loss of spin density due to the spin relaxation. Additionally, θ_s of Ta and $\text{Bi}_x\text{Se}_{(1-x)}$ are opposite, so the spin density generated by $\text{Bi}_x\text{Se}_{(1-x)}$ was cancelled.

One of the key factors for the widespread realization of SOT-based spintronic devices was the development of a spin channel with a high spin density-generation efficiency. Furthermore, the replacement of the FM by a ferromagnetic insulator avoids current shunting through the FM layer^{50,51}. This leads to a low J_{sw} of the adjacent magnet. Moreover, the development of a smooth NM interface at a low thermal budget must be achievable. We demonstrated the growth of smooth $\text{Bi}_x\text{Se}_{(1-x)}$ films on a large silicon wafer with a large θ_s using a semiconductor-industry compatible sputtering process. These films possess comparable or better σ_s compared to other reported spin density generators at RT^{3,6,16,30,31,36}. The polycrystalline nature of the sputtered $\text{Bi}_x\text{Se}_{(1-x)}$ films was found and confirmed by quantum transport simulations to be the key for the high SOT due to the quantum confinement effect. Furthermore, we developed and switched a perpendicular CoFeB multilayer on $\text{Bi}_x\text{Se}_{(1-x)}$ films at RT by a TI material, which enabled a path for reliable and efficient beyond-complementary metal-oxide semiconductor devices. The reported preliminary results of polycrystalline $\text{Bi}_x\text{Se}_{(1-x)}$ in this study have not been optimized, and we expect future developments, such as to explore the different crystalline orientations or chemical compositions, to bring further improvements.

Note added in proof: While our manuscript was under review a theoretical report⁵² predicted that an amorphous system can have topologically non-trivial states and an experimental report⁵³ demonstrated that topological surface states can exist in granular TI.

Methods

Methods, including statements of data availability and any associated accession codes and references, are available at <https://doi.org/10.1038/s41563-018-0136-z>.

Received: 4 July 2017; Accepted: 21 June 2018;

Published online: 30 July 2018

References

- Hasan, M. Z. & Kane, C. L. Colloquium: topological insulators. *Rev. Mod. Phys.* **82**, 3045–3067 (2010).
- Zhang, H. et al. Topological insulators in Bi_2Se_3 , Bi_2Te_3 and Sb_2Te_3 with a single Dirac cone on the surface. *Nat. Phys.* **5**, 438–442 (2009).
- Mellnik, A. R. et al. Spin-transfer torque generated by a topological insulator. *Nature* **511**, 449–451 (2014).
- Fan, Y. et al. Magnetization switching through giant spin-orbit torque in a magnetically doped topological insulator heterostructure. *Nat. Mater.* **13**, 699–704 (2014).
- Kondou, K. et al. Fermi-level-dependent charge-to-spin current conversion by Dirac surface states of topological insulators. *Nat. Phys.* **12**, 1027–1032 (2016).
- Wang, Y. et al. Topological surface states originated spin-orbit torques in Bi_2Se_3 . *Phys. Rev. Lett.* **114**, 257202 (2015).
- Li, C. H. et al. Electrical detection of charge-current-induced spin polarization due to spin-momentum locking in Bi_2Se_3 . *Nat. Nanotech.* **9**, 218–224 (2014).
- Ando, Y. et al. Electrical detection of the spin polarization due to charge flow in the surface state of the topological insulator $\text{Bi}_{1-x}\text{Sb}_x\text{Te}_{1-x}\text{Se}_x$. *Nano Lett.* **14**, 6226–6230 (2014).
- Chen, Y. L. et al. Experimental realization of a three-dimensional topological insulator, Bi_2Te_3 . *Science* **325**, 178–180 (2009).
- Pan, Z.-H. et al. Electronic structure of the topological insulator Bi_2Se_3 using angle-resolved photoemission spectroscopy: evidence for a nearly full surface spin polarization. *Phys. Rev. Lett.* **106**, 257004 (2011).
- Manchon, A. et al. Current-induced spin-orbit torques in ferromagnetic and antiferromagnetic systems. Preprint at <http://arXiv.org/cond-mat.mes-hall/1801.09636> (2018).
- Jamali, M. et al. Giant spin pumping and inverse spin Hall effect in the presence of surface and bulk spin-orbit coupling of topological insulator Bi_2Se_3 . *Nano Lett.* **15**, 7126–7132 (2015).
- Shiomi, Y. et al. Spin-electricity conversion induced by spin injection into topological insulators. *Phys. Rev. Lett.* **113**, 196601 (2014).
- Deorani, P. et al. Observation of inverse spin Hall effect in bismuth selenide. *Phys. Rev. B* **90**, 94403 (2014).
- Rojas-Sánchez, J.-C. et al. Spin to charge conversion at room temperature by spin pumping into a new type of topological insulator: α -Sn films. *Phys. Rev. Lett.* **116**, 96602 (2016).
- Liu, L. et al. Spin-torque switching with the giant spin Hall effect of tantalum. *Science* **336**, 555–558 (2012).
- Manchon, A. & Zhang, S. Theory of spin torque due to spin-orbit coupling. *Phys. Rev. B* **79**, 94422 (2009).
- Suzuki, T. et al. Current-induced effective field in perpendicularly magnetized Ta/CoFeB/MgO wire. *Appl. Phys. Lett.* **98**, 142505 (2011).
- Miron, I. M. et al. Perpendicular switching of a single ferromagnetic layer induced by in-plane current injection. *Nature* **476**, 189–193 (2011).
- Manchon, A., Koo, H. C., Nitta, J., Frolov, S. M. & Duine, R. A. New perspectives for Rashba spin-orbit coupling. *Nat. Mater.* **14**, 871–882 (2015).
- Slonczewski, J. C. Current-driven excitation of magnetic multilayers. *J. Magn. Magn. Mater.* **159**, L1–L7 (1996).
- Chappert, C., Fert, A. & Van Dau, F. N. The emergence of spin electronics in data storage. *Nat. Mater.* **6**, 813–823 (2007).
- Brataas, A. & Hals, K. M. D. Spin-orbit torques in action. *Nat. Nanotechnol.* **9**, 86–88 (2014).
- Pai, C. F. et al. Spin transfer torque devices utilizing the giant spin Hall effect of tungsten. *Appl. Phys. Lett.* **101**, 122404 (2012).
- Manipatruni, S., Nikonov, D. E. & Young, I. A. Energy-delay performance of giant spin Hall effect switching for dense magnetic memory. *Appl. Phys. Express* **7**, 103001 (2014).
- Kim, J. et al. Layer thickness dependence of the current-induced effective field vector in Ta[CoFeB]MgO. *Nat. Mater.* **12**, 240–245 (2013).
- Zhao, Z., Jamali, M., Smith, A. K. & Wang, J. P. Spin Hall switching of the magnetization in Ta/TbFeCo structures with bulk perpendicular anisotropy. *Appl. Phys. Lett.* **106**, 132404 (2015).
- Hao, Q. & Xiao, G. Giant spin Hall effect and switching induced by spin-transfer torque in a $\text{W/Co}_{40}\text{Fe}_{40}\text{B}_{20}/\text{MgO}$ structure with perpendicular magnetic anisotropy. *Phys. Rev. Appl.* **3**, 34009 (2015).
- Liu, L., Lee, O. J., Gudmundsen, T. J., Ralph, D. C. & Buhrman, R. A. Current-induced switching of perpendicularly magnetized magnetic layers using spin torque from the spin Hall effect. *Phys. Rev. Lett.* **109**, 96602 (2012).
- Han, J. et al. Room-temperature spin-orbit torque switching induced by a topological insulator. *Phys. Rev. Lett.* **119**, 77702 (2017).
- Wang, Y. et al. Room temperature magnetization switching in topological insulator-ferromagnet heterostructures by spin-orbit torques. *Nat. Commun.* **8**, 1364 (2017).
- Kawaguchi, M. et al. Current-induced effective fields detected by magnetotransport measurements. *Appl. Phys. Express* **6**, 113002 (2013).
- Liu, L., Moriyama, T., Ralph, D. C. & Buhrman, R. A. Spin-torque ferromagnetic resonance induced by the spin Hall effect. *Phys. Rev. Lett.* **106**, 36601 (2011).
- Xu, W. J. et al. Scaling law of anomalous Hall effect in Fe/Cu bilayers. *Eur. Phys. J. B* **65**, 233–237 (2008).
- Şahin, C. & Flatté, M. E. Tunable giant spin Hall conductivities in a strong spin-orbit semimetal: $\text{Bi}_{1-x}\text{Sb}_x$. *Phys. Rev. Lett.* **114**, 107201 (2015).

36. Zhang, W., Han, W., Jiang, X., Yang, S.-H. & Parkin, S. S. P. Role of transparency of platinum–ferromagnet interfaces in determining the intrinsic magnitude of the spin Hall effect. *Nat. Phys.* **11**, 496–503 (2015).
37. Ashcroft, N. W. & Mermin, N. D. *Solid State Physics* (Brooks-Cole, Grove, 1976).
38. Kobayashi, K. Electron transmission through atomic steps of Bi₂Se₃ and Bi₂Te₃ surfaces. *Phys. Rev. B* **84**, 205424 (2011).
39. Edelstein, V. M. Spin polarization of conduction electrons induced by electric current in two-dimensional asymmetric electron systems. *Solid State Commun.* **73**, 233–235 (1990).
40. Ndiaye, P. B. et al. Dirac spin–orbit torques and charge pumping at the surface of topological insulators. *Phys. Rev. B* **96**, 14408 (2017).
41. Ghosh, S. & Manchon, A. Spin–orbit torque in a three-dimensional topological insulator–ferromagnet heterostructure: crossover between bulk and surface transport. *Phys. Rev. B* **97**, 134402 (2018).
42. Fischer, M. H., Vaezi, A., Manchon, A. & Kim, E.-A. Spin-torque generation in topological insulator based heterostructures. *Phys. Rev. B* **93**, 125303 (2016).
43. Mahfouzi, F., Nikoli, B. K. & Kioussis, N. Antidamping spin–orbit torque driven by spin–flip reflection mechanism on the surface of a topological insulator: a time-dependent nonequilibrium Green function approach. *Phys. Rev. B* **93**, 115419 (2016).
44. Kurebayashi, H. et al. An antidamping spin–orbit torque originating from the Berry curvature. *Nat. Nanotech.* **9**, 211–217 (2014).
45. Bahramy, M. S. et al. Emergent quantum confinement at topological insulator surfaces. *Nat. Commun.* **3**, 1159 (2012).
46. Avci, C. O. et al. Interplay of spin–orbit torque and thermoelectric effects in ferromagnet/normal-metal bilayers. *Phys. Rev. B* **90**, 224427 (2014).
47. Pai, C.-F., Mann, M., Tan, A. J. & Beach, G. S. D. Determination of spin torque efficiencies in heterostructures with perpendicular magnetic anisotropy. *Phys. Rev. B* **93**, 144409 (2016).
48. Cao, J. et al. Spin–orbit torques induced magnetization reversal through asymmetric domain wall propagation in Ta/CoFeB/MgO structures. *Sci. Rep.* **8**, 1355 (2018).
49. Rojas-Sánchez, J.-C. et al. Spin pumping and inverse spin Hall effect in platinum: the essential role of spin-memory loss at metallic interfaces. *Phys. Rev. Lett.* **112**, 106602 (2014).
50. Avci, C. O. et al. Current-induced switching in a magnetic insulator. *Nat. Mater.* **16**, 309–314 (2016).
51. Li, P. et al. Spin–orbit torque-assisted switching in magnetic insulator thin films with perpendicular magnetic anisotropy. *Nat. Commun.* **7**, 12688 (2016).
52. Agarwala, A. & Shenoy, V. B. Topological insulators in amorphous systems. *Phys. Rev. Lett.* **118**, 236402 (2017).
53. Banerjee, A. et al. Granular topological insulators. *Nanoscale* **9**, 6755 (2017).

Acknowledgements

We thank P. Crowell for proofreading the manuscript and M. Kawaguchi for helpful discussions on data analysis. We also thank T. Peterson and G. Stecklein for their help with the PPMS measurements. This work was supported by C-SPIN, one of six STARnet programme research centres. This work utilized (1) the College of Science and Engineering (CSE) Characterization Facility, University of Minnesota (UM), supported in part by the NSF through the UMN MRSEC programme (no. DMR-1420013), and (2) the CSE Minnesota Nano Center, UM, supported in part by the NSF through the NNIN programme. A.M. was supported by the King Abdullah University of Science and Technology (KAUST).

Author Contributions

J.P.W., M.D.C. and M.J. designed the experiments. J.-Y.C., M.J. and D.Z. grew the samples. M.D.C., M.J., Z.Z., H.L., D.Z. and Y.L. designed the experimental set-up. M.D.C., H.L. and Z.Z. performed the fabrication of the devices and electrical measurements. J.P.W. proposed the study of the grain-dependent quantum confinement effect on the sputtered Bi₂Se_(1-x) films. R.G., T.L. and A.M. carried out the theoretical modelling. D.R.H. and K.A.M. performed the STEM. M.D.C., D.Z. and P.Q. did data analysis. M.D.C. and J.P.W. wrote the manuscript, and all the authors discussed the results, contributed to the draft of the manuscript and commented on the final version. J.P.W. coordinated the overall project.

Competing interests

The authors declare no competing interests.

Additional information

Supplementary information is available for this paper at <https://doi.org/10.1038/s41563-018-0136-z>.

Reprints and permissions information is available at www.nature.com/reprints.

Correspondence and requests for materials should be addressed to J.-P.W.

Publisher's note: Springer Nature remains neutral with regard to jurisdictional claims in published maps and institutional affiliations.

Methods

Sample growth and thin-film characterization. All of the $\text{Bi}_x\text{Se}_{(1-x)}$ thin films were grown on Si/SiO₂ substrates at RT by sputtering a composite Bi_2Se_3 (99.99% pure) target in our ultrahigh vacuum six-target Shamrock sputtering system with a base pressure of 5.0×10^{-8} Torr. Bi_2Se_3 was sputtered at a 50 W d.c. power and a 3 mTorr Ar pressure to yield a deposition rate of 0.7 \AA s^{-1} . The MgO layer was radiofrequency sputtered at a deposition rate of 0.07 \AA s^{-1} , whereas all of the metallic layers (Ta, CoFeB and Gd) were d.c. sputtered at an Ar pressure of 3 mTorr. VSM and AFM were used to characterize the magnetic properties and surface roughness, respectively. For STEM measurements, an aberration-corrected (using a CEOS DCOR probe corrector) FEI Titan G2 60–300S/TEM equipped with a Schottky X-FEG gun was used, operated at 200 kV with a convergence angle of 16 mrad.

Device fabrication and electrical characterization. The multilayer thin films patterned into Hall-cross bars of width 5–30 μm and length 70 μm were fabricated by using an optical lithography process for the Hall measurement. After the first step of photolithography, the Ar ion mill was used to define the Hall-cross bars. Ti(10 nm)/Au(120 nm) electrical contacts were deposited after the second step of lithography using an electron-beam evaporator. A physical property measurement system (PPMS) was used to measure the electrical properties. Keithley's 2182 nanovoltmeter and 6221 current source were used to probe the voltage and supply current, respectively.

Numerical simulations. Quantum transport simulations (as well as calculations of the equilibrium properties in Fig. 3b–d) were performed within the non-equilibrium Green's functions approach⁵⁴ using the same atomistic sp^3 tight-binding Hamiltonian as in Edelstein³⁹. All three geometries (slab, wire and dot) were simulated by considering a simulation domain of finite length L_x in the transport direction, but with different boundary conditions. In the slab and wire cases, semi-infinite leads were applied and the corresponding self-energies calculated using a known iterative algorithm. In the dot case, a phenomenological self-energy that corresponded to a contact-induced energy broadening of 1 eV was added to the on-site energies of the atomic orbitals that belonged to the left and right, that is, $(\bar{1}10)$ surfaces. This allowed us to distinguish between the contributions of forward and backward propagating states.

Equilibrium quantities were calculated assuming a flat electrostatic potential profile. The expression for the spin density spectrum $S_y^+(E)$ in terms of Green's functions is provided in the main text. As for the density of states, we used:

$$D(E) = \frac{1}{2\pi L_x L_y L_z} \text{Tr} [G^R (I_1 + I_2) G^A]$$

where L_z is the TI thickness and the other symbols are as defined below. Transport results at a finite electric field were obtained by applying a small voltage V across

the left and right contacts, such that the current is in the linear regime, and by including a linear potential profile along the x direction. Results at finite V but zero electric field were obtained by approximating S_y and I_c as:

$$S_y = e \int_{-\infty}^{\infty} dE S_{y,0}^+(E) \left(\frac{-\partial f_0}{\partial E} \right) V$$

$$I_c = \frac{e^2}{h} \frac{1}{L_y} \int_{-\infty}^{\infty} dE T_0(E) \left(\frac{-\partial f_0}{\partial E} \right) V$$

where the subscript 0 stresses the fact that the quantities are calculated in equilibrium condition.

The spin accumulation per unit area on the top surface was computed as:

$$S_y = \int_{-\infty}^{\infty} dE [S_y^+(E) f_1(E) + S_y^-(E) f_2(E)]$$

where $f_{1,2}$ are the Fermi–Dirac distribution functions of the two contacts and

$$S_y^{\pm}(E) = \frac{1}{2\pi L_x L_y} \text{Tr} (G^R \Gamma_{1,2} G^A P \otimes \sigma_y)$$

where G^R and G^A are the retarded and advanced Green's function matrices, respectively, and $\Gamma_{1,2}$ are the broadening matrices that correspond to the left/right contacts. The charge current (per unit width) can be computed in a similar manner:

$$I_c = \frac{e}{h} \frac{1}{L_y} \int_{-\infty}^{\infty} dE T(E) [f_1(E) - f_2(E)]$$

where the transmission function $T(E)$ is given by $T(E) = \text{Tr} [I_1^R G^R I_2^A G^A]$. A bias of $V = 0.01 \text{ V}$ was applied between the Fermi levels of the left and right contacts and a corresponding uniform electric field $F = V/L_x$ was imposed along x . We also compared the results for the case in which a small V was applied but $F = 0$, with insignificant differences revealed.

Data availability. The data that support the findings of this study are available from the corresponding authors on reasonable request.

References

54. Datta, S. *Electronic Transport in Mesoscopic Systems* (Cambridge Univ. Press, Cambridge, 1995).